

Creep Rheology of Antigorite: Experiments at Subduction Zone Conditions

Eric Burdette¹ and Greg Hirth¹

¹Brown University

November 22, 2022

Abstract

Novel fluid medium pressure cells were used to deform antigorite under constant stress creep conditions at low temperature, low strain rate (10^{-9} - 10^{-4} 1/s), and high pressure (1 GPa) in a Griggs-type apparatus. Antigorite cores were deformed at constant temperatures between 75°C and 550°C, applying 8-12 stress-strain steps per temperature. The microstructures of deformed samples highlight the importance of basal shear and kinks to antigorite plasticity. Rheological data were fit with a low temperature plasticity law, consistent with a deformation mechanism involving large lattice resistance. When applied at geologic stresses and strain rates, the extrapolated viscosity agrees well with predictions based on subduction zone thermal models.

Creep Rheology of Antigorite: Experiments at Subduction Zone Conditions

Eric Burdette and Greg Hirth

¹Department of Earth, Environmental and Planetary Sciences, Brown University, Providence, RI, USA

Key Points:

- Isotropic antigorite was deformed at constant stress to low strain
- Slip along basal planes and kinks allow plastic deformation
- A low temperature plasticity (LTP) creep law describes deformation rheology well

Corresponding author: Eric Burdette, eric.burdette@brown.edu

Abstract

Novel fluid medium pressure cells were used to deform antigorite under constant stress creep conditions at low temperature, low strain rate (10^{-9} – 10^{-4} 1/s), and high pressure (1 GPa) in a Griggs-type apparatus. Antigorite cores were deformed at constant temperatures between 75°C and 550°C, applying 8–12 stress-strain steps per temperature. The microstructures of deformed samples highlight the importance of basal shear and kinks to antigorite plasticity. Rheological data were fit with a low temperature plasticity law, consistent with a deformation mechanism involving large lattice resistance. When applied at geologic stresses and strain rates, the extrapolated viscosity agrees well with predictions based on subduction zone thermal models.

Plain Language Summary

Antigorite is a hydrous mineral that is present on top of subducting slabs and in stagnant mantle wedge whose rheology could control subduction structure. Instead of deforming antigorite with our motor set to constant speed, we redesigned the deformation assembly and machine to accurately servo-control the stress on deforming samples. Measuring strain rate at several stresses and temperatures allows us to construct a flow law to extrapolate behavior to subduction stresses/strain rates. The microstructure of samples cut open after deformation suggests resistance of defect movement along the crystallographic sheets controls rheology.

1 Introduction

Subduction zones are among the most seismically active tectonic environments on Earth. The wide spectrum of brittle and ductile behavior in the down-going slab and nearby mantle control seismic coupling, deep fluid transport, and local mantle convection. The interplay between rheology and metamorphic reactions is key to understanding tectonic dynamics and evolution of subduction structure at depth. To explain a range of observations from subduction zones (e.g., heat flow, location of volcanic front, slab seismicity, seismic structure of the mantle wedge), thermal models require slab decoupling from the mantle wedge down to a depth of approximately 80 km (e.g. Wada et al., 2008; Syracuse et al., 2010). Owing to its relative weakness compared to other lithospheric minerals, the presence of serpentine along the interface has been called on to promote this decoupling (e.g. Wada & Wang, 2009). In altered oceanic lithosphere and mantle wedge, antigorite is the stable serpentine polytype at these high pressure/high temperature conditions (Wunder & Schreyer, 1997; Schwartz et al., 2013).

The rheology of antigorite at high pressure has been investigated in a wide range of experimental studies. Flow laws constrained by strain rate stepping experiments from these studies have reported both dislocation creep behavior ($\dot{\epsilon} \propto \sigma^n$, with $n = 3 - 4$ (Hilaret et al., 2007; Auzende et al., 2015)) and/or flow laws with greater stress-dependence consistent with low-temperature plasticity or semi-brittle flow (effective $n > 10$ (Chernak & Hirth, 2010; Proctor & Hirth, 2016; Shao et al., 2021; Hirauchi et al., 2020)). Such large variation in estimated stress-dependence leads to large uncertainties when extrapolating flow laws to the relevant geologic conditions. The uncertainty in the extrapolation can be resolved by conducting deformation experiments at strain rates lower than previously examined experimentally (almost all previously published data were collected at constant strain rates greater than 10^{-6} 1/s). For low strain rate deformation, constant-stress creep tests are generally advantageous because deformation typically approaches steady-state over a small strain interval, allowing mechanical measurements of lower strain rates than is practical during constant strain-rate tests. However, constant-stress experiments also present technical challenges, which necessitated the development of new experimental approaches for our study.

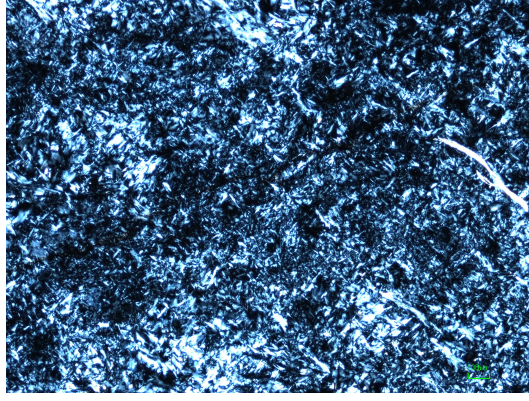


Figure 1. Thin section image (cross-polarized) of the starting material's undeformed mesh texture. Compression of samples was in the vertical direction.

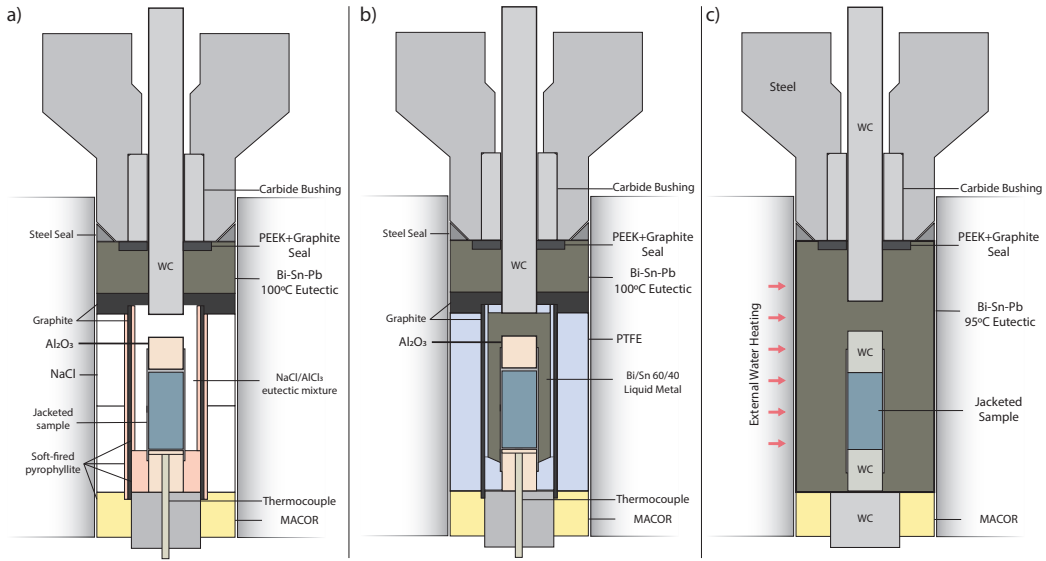


Figure 2. Sample assemblies used in this work. a) High temperature partially molten salt assembly, b) Teflon (PTFE) lined liquid metal assembly, c) Eutectic alloy assembly (externally heated).

We conducted creep tests on solid cores of mesh-textured antigorite at constant differential stress. To improve the resolution of both stress and strain rate we redesigned the dynamic seals, sample assembly, and mechanical control of a Griggs-type deformation apparatus (Burdette, 2021) optimized for the relatively low temperature conditions where antigorite is stable. The microstructures preserved after deformation are not dominated by cataclastic flow and provide evidence for the important contribution of basal slip and kinking to strain accommodation.

2 Materials, Cell Designs, and Methods

2.1 Materials and Sample Preparation

Antigorite samples were cored from a serpentinite collected from the Nagasaki metamorphic belt in Japan; this material (which was also used in the studies of Proctor and

Table 1. List of Experiments

Experiment	Sample	Temperature (°C)	Pressure (MPa)	Confining Media	Strain
W2394-75	Westerly Granite	75	200	95C Alloy	0.04
W2424-550	Antigorite	550	1000	NaCl-AlCl ₃	0.02
W2439-400	Antigorite	400	1000	NaCl-AlCl ₃	0.04
W2441-75	Antigorite	75	1000	95C Alloy	0.05
W2447-200	Antigorite	200	1000	60:40 Bi:Sn	0.04
W2520-520	Antigorite	520	1000	NaCl-AlCl ₃	0.02
W2521-75	Antigorite	75	1000	Hydraulic Oil	0.03
W2526-480	Antigorite	480	1000	NaCl-AlCl ₃	0.01

Hirth (2015) and Okazaki and Hirth (2016)) is predominantly antigorite (98%) with minor diopside, spinel and magnetite. The original microstructure of cored samples shows a generally isotropic, interpenetrating mesh texture (Wicks & Whittaker, 1977) which results in many antigorite grains oriented around 45 degrees to the axial compression direction (Figure 1). However, there is no macroscopic foliation.

2.2 Sample Assemblies

Constant-stress experiments present technical challenges, which necessitated the development of new experimental approaches for our study. Samples were jacketed in thin copper or silver sleeves and deformed at 1 GPa confining pressure in one of three modified Griggs-type deformation assemblies, depending on the experimental temperature (Figure 2). For $T \geq 400^\circ\text{C}$, a eutectic partial melt salt (0.15AlCl₃-0.85NaCl mol, which produces 15+% melt during experiments) was used in a molten salt assembly (Figure 2a). For $T=200^\circ\text{C}$, a modified molten salt assembly was fabricated with molten Bi-Sn alloy replacing the inner salt, and machined Teflon replacing pyrophyllite (Figure 2b). For experiments at $T=75^\circ\text{C}$, a weak Bi-Sn-Pb eutectic (95°C) alloy was cast into a tube filling the space between samples and the pressure vessel walls (Figure 2c). The entire pressure vessel and cell were heated above 75°C by flowing hot water through the standard cooling rings, causing the confining alloy to become very weak and presenting low resistance to sample barreling and piston advancement.

The incorporation of fluid components into the assembly motivated the use of axial thermocouples placed below the sample, rather than a radial thermocouple entering through the furnace towards the center of the sample. Thermal modeling (Moarefvand et al., 2021; Burdette, 2021, section C.1) and previous studies (Kirby & Kronenberg, 1984) indicate that the axial thermocouple measures a 10°C colder area of the sample column, representing a more reliable, but also lower bound on the sample temperature.

Low dynamic friction is critical for characterizing samples with large stress sensitivity. To decrease friction, we replaced the beveled mitre-ring seal used in Griggs-type apparatuses with a tight-tolerance polished carbide bushing and graphite-filled PEEK washer (Figure 2). This design limits extrusion of seal material and promotes excellent piston alignment. We tested the new design by conducting tests on brass using paraffin wax as a confining medium (Burdette, 2021, Figure 2.16). With these improvements, both the magnitude and rate-dependence of dynamic seal friction were reduced by approximately a factor of five.

Acoustic emission data were acquired using a piezoelectric transducer located in the base plate, below the sample assembly (Okazaki et al., 2021).

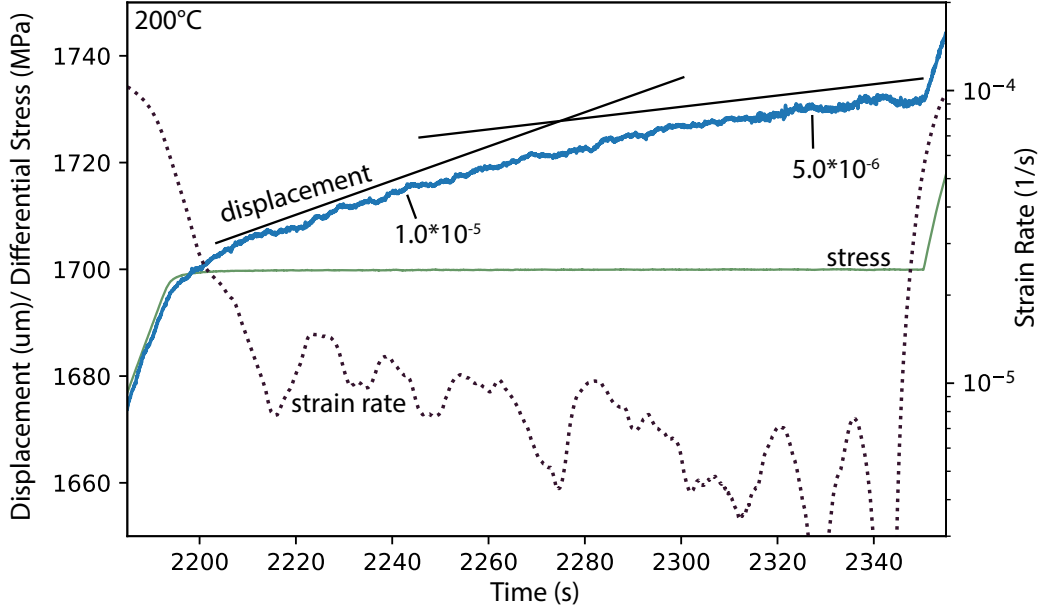


Figure 3. Antigorite creep stress, displacement, and strain rate plotted against time to show strain rate evolution during a stress step. Data for plotting and fitting is taken from the final portion of the displacement curve.

2.3 Stress Stepping Methods

In all creep experiments on antigorite cores, the deformation piston was first advanced until it “hit” the sample and loaded to starting stress. The sample was then allowed to creep at constant stress for 2-24 hours (these data would potentially be impacted by a number of issues, including squeeze-out of metal foil between sample and piston, thermal equilibration, and relaxation of stresses in the assembly, and were conservatively not used in the determination of flow laws). For each subsequent stress step, strain rate was monitored and allowed to stabilize after reaching the target stress. Examples of transients observed at low strain after the achievement of a target stress are illustrated in Figure 3. Strain rate data for plotting was taken from strain recorded at the end of each step.

To test the performance of the new dynamic seal, we also conducted stress stepping creep tests on Westerly granite at confining pressure of 200 MPa and temperature of 75°C in the low temperature assembly and compared the results to published data acquired in a gas-confining medium apparatus (Brantut et al., 2012). As shown in Figure 4 our data compare favorably and show good agreement with previous work for strain rates down to 5×10^{-8} /s.

3 Results

3.1 Mechanical Results

The creep rate of antigorite systematically increases with increasing temperature and exhibits a stress dependence that decreases with temperature. As shown in Figure 5b, For strain rates $> 10^{-6}$ 1/s, data for a given temperature show a nominally constant

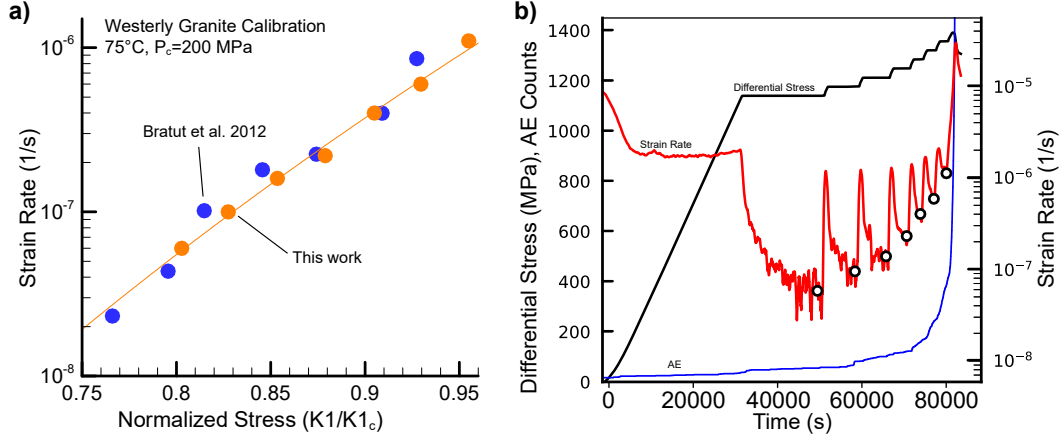


Figure 4. Data recorded during the cross-validation creep test on Westerly granite. Points denote the measured strain rates after the specimen has reached nominal steady state. Acoustic emission (AE) data are counts/hits of events recorded during the experiment.

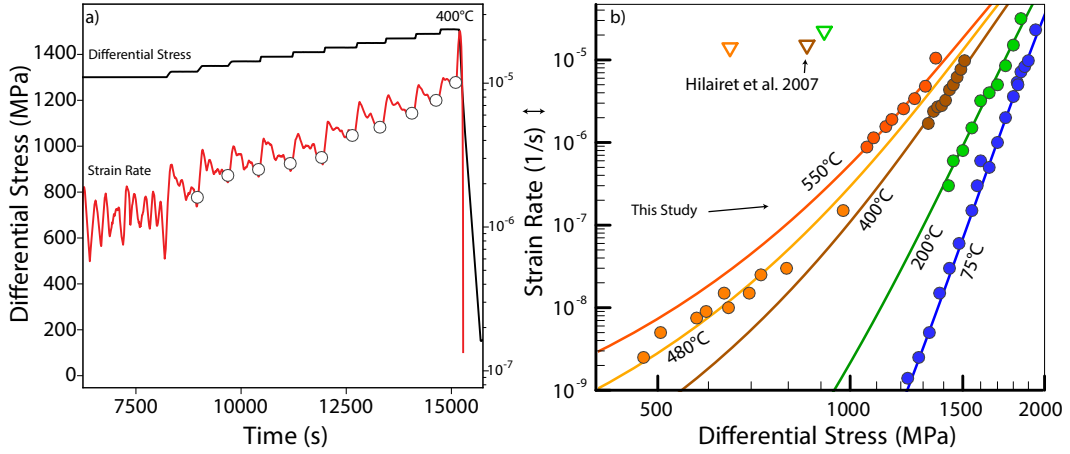


Figure 5. a) Stress and strain rate data from the antigorite creep test at 400°C. Circles are final strain rate data. (Note that these circles cover a smaller range than the plot of combined data) b) Final strain rate plotted against differential stress (this study, circles). Colors denote temperature matched curves from the global low temperature plasticity creep fit. Data of Hilaret et al. (2007) are included as open inverted triangles for reference.

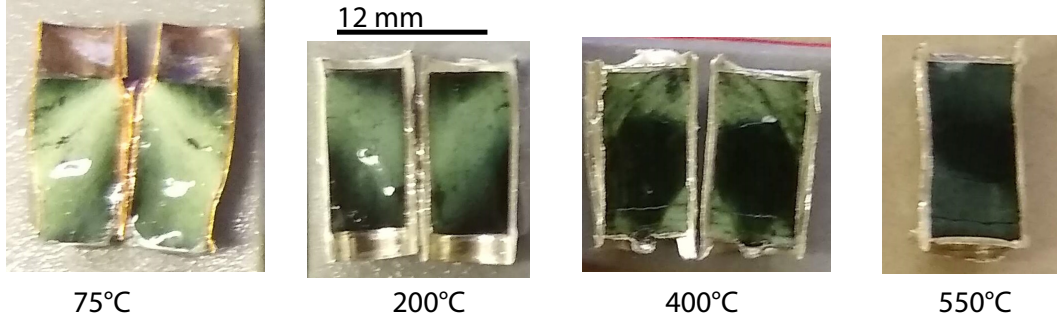


Figure 6. Images of deformed antigorite core macrostructure. Comparison with SEM imaging indicates that light/white portions of samples have a higher density of shear microcracks. Samples are initially dark green/black.

stress exponent, varying from $n \approx 20$ at 75°C to $n \approx 5$ at 550°C. Inspection of data from the highest temperatures illustrates a decrease in n below strain rate of 10^{-7} 1/s. The fit to a low temperature plasticity flow law is plotted in Figure 5 and discussed in section 4.1. A list of experiments is included in Table 1. Stress, strain rate, and strain data are included in supplementary material.

We monitored acoustic emission (AE) activity during the antigorite creep experiments, and emissions were not detected during creep tests (e.g. Okazaki & Hirth, 2016; Gasc et al., 2017; Ferrand et al., 2017). In contrast, we observed hundreds of emissions during our creep test on Westerly granite, with an event frequency that increased proportional to strain rate (Figure 4).

3.2 Deformation Microstructure

Microstructures within the mesh texture provide evidence that basal slip along the antigorite grains leads to interactions between grains in the opposing sheets of the local mesh texture (X-shaped structures). As described next, these textures vary with temperature. Sample scale photos of the deformed samples are included in Figure 6. Shear microcracks decorate deformed regions of samples and scatter light to appear brighter in sample-scale images.

Samples deformed at 75°C exhibit deformation primarily along a 1 mm wide, banded structure oriented 35 degrees from the axial compression direction (Figure 6). Within the deformation zone, we observed $< 200\mu\text{m}$ shear cracks and a high density of relatively tight kinks (Figure 7c); there is little other evidence for comminution/damage in the localized zone. We define kink angle as deviation from an unkinked plane (180 degrees less/minus the inner "opening" angle between the traces of visible cleavage planes) so that slight bending corresponds to a small kink angle. The average kink angle at 75°C is 54° (29 measurements, minimum 40°, maximum 68°). This value is approximately twice the period doubling angle (defining the angle between the orientation of the radius of curvature of the adjacent segments of the alternating antigorite structure) observed in polygonal serpentinite samples (Grobety, 2003).

The core deformed at 200°C also displays deformation marked by shear microcracks at 35 degrees to axial compression, but the deformed zone is wider (2 mm width, Figure 7a). Kinks are visible throughout the deformed zone and are present at the intersection of grains whose basal planes have opposing orientations for high shear stress ($\pm 45^\circ$), forming X-shaped structures (Figure 7b). When the kink angle is small (see Figure 7b),

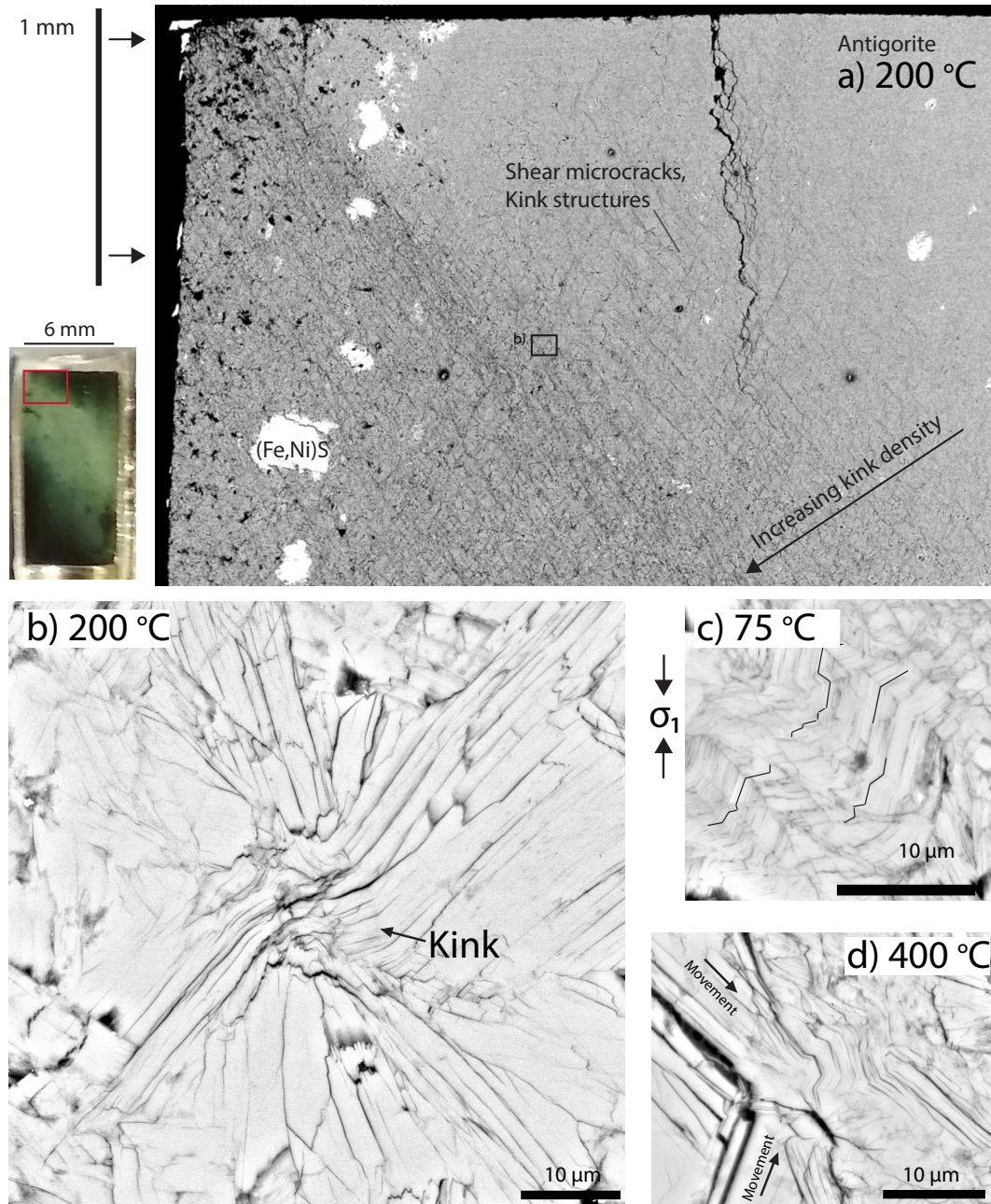


Figure 7. a) Image showing both macroscopic color image of damage (light color), and backscatter SEM image of the 200°C creep sample. The visible structures in SEM are X-shaped structures of opposing antigorite foliation. The opposing orientation leads to kinking at the intersection of opposing grains and delamination opening upon decompression around the kinked structures. b) Backscatter SEM image of X-shaped structures in the 200°C creep sample. Opposing orientation of the pictured grains forces kinking at the intersection, and eventual tearing when easy kinking is exhausted. C-axis (along sheet) deformation is required for this structure to form. Delamination cracks open after decompression due to residual stress. c) SEM Image of low temperature antigorite deformation microstructures. Tight kinks, with angles 2-3x higher than elevated temperatures are highlighted by black lines following the sheet basal planes. d) SEM Image of structures in the sample deformed at 400°C. Arrows denote movement of opposing grains along a cracked slip surface. Stress is concentrated at the intersection of the grains, resulting in four tight kinks. Note that kink angle and delamination decrease rapidly with distance from the intersection in contrast to lower temperature microstructure. Differential stress is vertical in all images.

the sheets mostly intact along their length. A collection of 9 measurements of average kink angles yielded an average angle of 23° (minimum 15°, maximum 33°).

At 400°C the deformation appears more distributed. Kinks and microcracks are distributed throughout the deformed area of the sample (bright in Figure 6). A lack of strain localization in core samples deformed to low strain at 400°C is consistent with previous work (Chernak & Hirth, 2010). X-shaped structures are also present in the most deformed parts of the sample, but they are less densely spaced than observed at lower temperature, and accordingly the kink density is lower in the sample deformed at 400°C. The kink angles vary as a function of distance from the stress concentrating grain intersections (Figure 7c). The average kink angle less than 10 μm from the annotated compression structure shown in Figure 7c is 45 degrees, while the kink angles 20 μm away are 10-20°. This observation indicates that the kink bands grow outward with increasing deformation at the stress-concentrating feature.

Samples deformed at 550°C also have X-shaped structures, and distributed deformation similar to the 400°C sample. However, we did not observe clear kinks. Bending of grains is observed, but only at small scales ($< 1\mu\text{m}$, included in supplement). Where these small bends in the grains appear, they do not have a clear apex as observed for lower temperate samples.

4 Discussion

The creep data in Figure 5b define a systematic stress dependence at each temperature. Variation in stress sensitivity (i.e. stress exponent) with increasing stress and temperatures is uniquely well described by a flow law used for barrier-controlled glide of dislocations. Here we discuss the fit and follow with a discussion of the deformation mechanisms, compare mechanisms and results to previous work, and note application to geologic conditions.

4.1 Low Temperature Plasticity Flow Law

Reduction of stress sensitivity (stress exponent) with increasing temperature is consistent with exponential low temperature plasticity (LTP) or 'barrier controlled' creep laws where stress or thermal activation allow defects to pass through the 'barrier'. LTP flow laws have the form (Frost & Ashby, 1982):

$$\dot{\epsilon} = A \left(\frac{\sigma}{\mu} \right)^2 \exp \left(\frac{-\Delta F}{RT} \left(1 - \left(\frac{\sigma}{\tau_0} \right)^p \right)^q \right) \quad (1)$$

Where A is a constant, σ is differential stress, μ is the shear modulus, ΔF is the activation energy required to overcome the obstacle without the aid of external stress, τ_0 is athermal flow stress, and are parameters that depend on the geometry of the barrier. A normalized σ^2 term accounts for the density of mobile dislocations in the sample.

The flow law parameters determined by fitting this LTP law are very sensitive to changes in the exponents p and q . The sensitivity to these exponents is not obvious at laboratory strain rates, but is clearly apparent in extrapolated strain rate and viscosity. We illustrate the problem with Figure 8b, where extrapolations of fits on A , ΔF , τ_0 at several values of p and q are displayed for data recorded at strain rates above 10^{-7} 1/s. Resulting uncertainty is also plotted in Figure 9a as a grey shaded region. Typically low temperature plasticity creep data do not extend below 10^{-7} 1/s (e.g. Evans & Goetze, 1979) due to the large required stresses, and these parameters are often assumed to both have values of 1.

However, as illustrated in Figure 8a, inclusion of data recorded at strain rates below 10^{-7} 1/s provides a constraint on these exponents. The data at the lowest strain rates

are better fit with $p = 1$ for all values of q . Based on this result, we fixed $p = 1$ in the inversion to reduce co-variance.

The best fit using all collected data gives a constant athermal flow stress (τ_0) = 2.42 ± 0.09 GPa, an inner exponent $p = 1$, an outer exponent $q = 1.18 \pm 0.09$, an activation energy $\Delta F = 86.3 \pm 2.9$ kJ/mol, and a pre-exponential constant A of $\exp(-0.624 \pm 0.236)$ 1/s. μ is assumed to be a constant at 35 GPa. Ranges noted are two standard deviations. Fits are also summarized in Table 2 where the values at the 2.5% and 97.5% percentiles of the posterior distributions are also noted. Further details of the Markov Chain Monte-Carlo fitting methods are provided in the supplemental information.

Table 2. Low temperature plasticity creep fit results

	Mean	Standard Deviation	hdi_2.5%	hdi_97.5%
$\ln(A) \ln(1/s)$	-0.624	0.118	-0.393	-0.859
ΔF (kJ)	86.3	1.4	83.4	89.1
τ_p (GPa)	2.42	0.04	2.33	2.50
q	1.18	0.05	1.08	1.27

4.2 Rate Limiting Deformation Mechanisms

The systematic variation of our data during individual tests and consistency with the LTP flow law suggest the creep rate is limited by a common underlying plastic mechanism over the explored range of conditions. For layered materials like antigorite, deformation is accommodated by basal shear mechanisms, which can involve sliding along shear microcracks or grain boundaries (e.g. 'asperity friction' Escartin et al., 1997; David et al., 2020; Idrissi et al., 2020), basal and sub-basal dislocations (e.g. (001), (101), and (10 $\bar{1}$) systems (Auzende et al., 2015; Amiguet et al., 2014)), or ripplocations (Gruber et al., 2016). The mechanical basis for the low temperature plasticity law suggests that moving defects along these crystallographic planes encounter a 'barrier' which can be overcome by stress or thermal activation. For antigorite the barrier could take one of several forms.

The simplest barrier would be a 'lattice resistance' to dislocation glide where the barrier is the energy required to break bonds and advance a dislocation by one unit cell dimension (Burgers vector). Antigorite has a structural corrugation in the a direction which defines a large unit cell (4.3, 0.9, 0.7 nm Bezacier et al., 2010); the volume (and thus activation area Hirth et al., 1983) is approximately an order of magnitude larger than that of forsterite, suggesting lattice resistance is plausible. The volume expansion required to advance defects across the corrugation (a direction) would be large. In contrast, slip in the b direction parallel to corrugation only requires breaking and re-forming four shared tetrahedral corner bonds. Proposed (101) and (10 $\bar{1}$) slip requires breaking many more octahedral bonds, but could still be possible as its burgers vector is small (0.9 nm Amiguet et al., 2014). Ripplocations would require even more volume expansion, which seems unlikely at 1+ GPa pressure.

TEM investigations of naturally and experimentally deformed samples highlight kink bands which have orientations consistent with slip along both a and b directions of intact sheets (Auzende et al., 2015, Figure 4e,f). However, during tensile in-situ TEM experiments (Idrissi et al., 2020), movement of dislocations is not observed as it is for other materials deformed using the same technique (Idrissi et al., 2016), and instead evidence for grain boundary sliding parallel to grain cleavage is observed.

Grain rotation could also lead to barriers to shear defect movement. Microstructures of deformed samples show formation of shear cracks along grains with high resolved shear stress (maximized for grains oriented 45 degrees to axial stress), and deformation of interpenetrating grains normal to shear cracks (Figure 7b-d). Rotation of grains between kink apexes (e.g. center of Figure 7b) reduces their resolved shear stress. Defects encountering the rotated plates would experience a large reduction in driving force which could act as a barrier to propagation of shear defects.

Kinking itself involves an organization of shear defects into lower energy configuration. This reduction of elastic strain energy provides the reduction or 'well' of an energy barrier. However, we do not see dense kink networks marked by shear cracks above 200°C, despite excellent fits to the same LTP law, which suggests lattice resistance mechanisms control deformation.

4.3 Effects of Temperature

Two related effects of temperature are illustrated by our results, and implied by the form of the LTP law: reduced stress dependence (exponent 'n') and more distributed deformation as a result. At high temperature the most likely mechanism to distribute deformation throughout samples is reduced lattice resistance along basal planes. Reduced lattice resistance allows shearing of grains with lower resolved shear stress throughout the samples, rather than only high resolved shear stress orientations. At the grain scale, reduced lattice resistance would lead to weaker sheet interaction, resulting in deformation of many zones along the length of a grain (distributed bending), rather than consolidation around the highest stress locations which can overcome the barrier to kinking and organize defects into a (e.g. dislocation) wall. This weakness at many locations along a grain would also lead to lower strength contrast between grains, especially those nearly perpendicular to one another as are pictured in Figure 7d.

Changes in stress sensitivity (stress exponent n) with temperature implied by the LTP creep law have been observed in another study (Shao et al., 2021). Their results show similar temperature sensitivity of strain rate to our results despite using oriented slices of strongly foliated antigorite deformed to 200%+ shear strain.

4.4 Shear Microcracks

Previous experimental work demonstrated that antigorite deforms by nominally non-dilatant, semi-brittle deformation mechanisms involving shear microcracks at confining pressures above 50 MPa (Escartin et al., 1997; David et al., 2018, 2020). Previous studies also show that the acoustic velocity of antigorite does not decrease after yielding (David et al., 2018), consistent with the nominally non-dilatant nature of deformation. There are a large number of shear microcracks visible in deformed specimens. We interpret that these shear cracks exist, but are closed during deformation, and "open" during depressurization of the samples, based on the lack of AE in our experiments and previous acoustic velocity data (i.e. David et al., 2018).

We observe shear cracks throughout our samples, but in contrast to some previous strain rate stepping studies (Hilaret et al., 2007; Chernak & Hirth, 2010; Proctor & Hirth, 2016), our microstructure is not dominated by cataclastic flow or comminution so we can consider the strain rates that we measure to be a result of plastic mechanisms (bending, kinking, grain boundary sliding) that share a common defect origin (e.g. dislocations or ripplocations).

Shear cracks distributed throughout our samples likely have some contribution to sample strength even if they are closed. They form along cleavage/basal planes so are likely to have low roughness. It is possible that, as David et al. (2020) and Hansen et al. (2020) describe, shear microcracks accommodate a significant portion of the deformation.

292 mation. The rate limiting mechanism of friction between two mated sheet surfaces (real
 293 fractional area of contact near 1) at 1 GPa could be similar to intrinsic lattice resistance
 294 discussed in the previous sections. Application of asperity plasticity to describe friction
 295 has successfully been used for olivine at high temperature (e.g. Boettcher et al., 2007;
 296 King & Marone, 2012). Further exploration of these sorts of observations could provide
 297 new insights into application of asperity models to explain frictional behavior at high
 298 pressures.

299 4.5 Effect of Texture

300 Our conclusion that deformation is limited by lattice resistance of defects slipping
 301 along basal planes is consistent with previous work on the influence of texture on the strength
 302 of antigorite aggregates. Our nominally isotropic antigorite starting material does not
 303 have the continuous “bladed band” structure present in many other serpentinites (Escartin
 304 et al., 1997), and instead has many sets of interpenetrating antigorite grains. This in-
 305 terlocking microstructure is possibly the strongest texture because basal shear is regu-
 306 larly impeded by grains perpendicular to the slip direction. Cores with texture aligned
 307 at 45 degrees to axial stress are weaker, and the effect of texture is more apparent at high
 308 temperature (Escartin et al., 1997; Chernak & Hirth, 2010; Hirauchi et al., 2020; Shao
 309 et al., 2021).

310 Despite the expected strong effect of texture, other experimental results have strength
 311 within 25% of our results. The only other test below strain rates of 10^{-6} are published
 312 in Proctor and Hirth (2016), whose data on mature, sheared gouge at 1 GPa falls within
 313 experimental error to predictions from flow law fits (comparisons included in supplement).

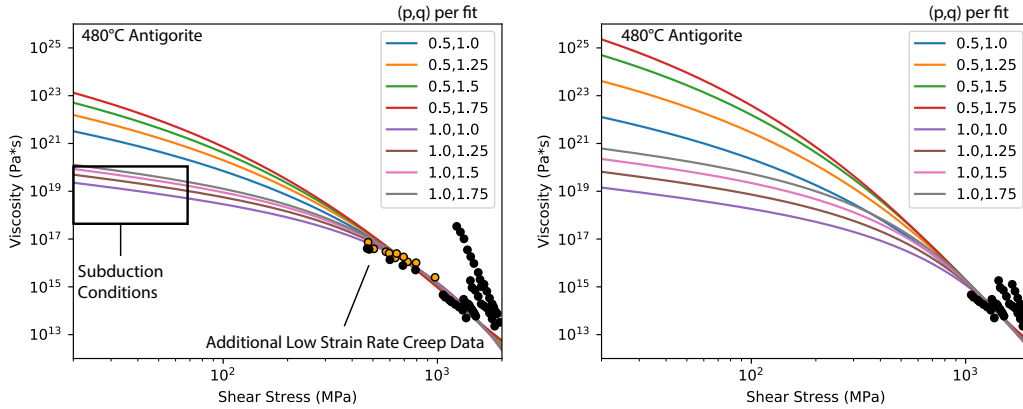


Figure 8. Comparison of extrapolated viscosity of the LTP law fit with fixed exponent p,q combinations with, and without slow strain rate data ($\dot{\epsilon} 10^{-7}$ 1/s) included in the fitted dataset (for illustration). Data at 480°C is plotted in orange, while data for all other temperatures is plotted in black.

314 4.6 Geodynamic Implications of Flow Law Parameter Results

315 Thermal modeling of subduction zones suggests a 100m thick layer of weak ma-
 316 terial at the slab surface would require viscosity between 10^{19} and $10^{18} Pa \cdot s$ to match
 317 heat flow measurements constraining mantle decoupling depths (Wada et al., 2008). At
 318 400°C and a shear stress of 50 MPa, our results predict a viscosity of $10^{19.5} Pa \cdot s$ and
 319 at 600°C they predict viscosity of $10^{18.0} Pa \cdot s$ (deviatoric stress/strain rate to match Wada
 320 et al. (2008)). Extrapolation after conversion is presented in Figure 9b. The difference

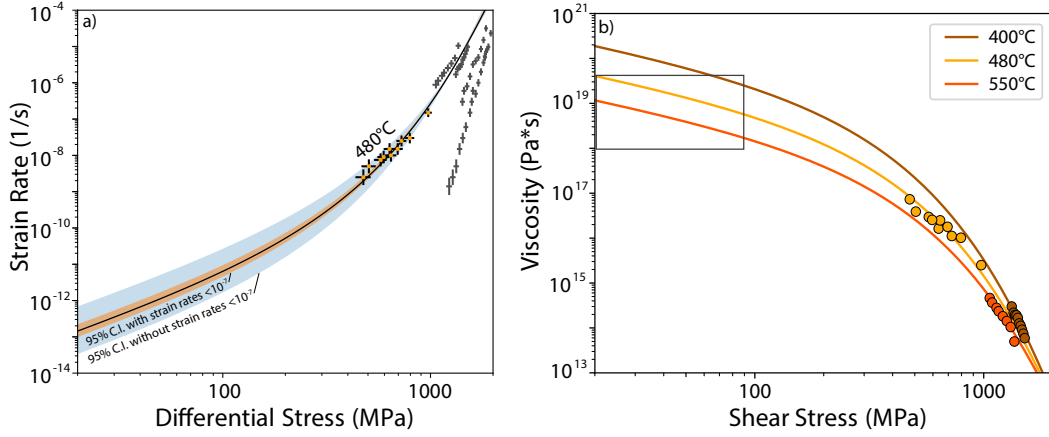


Figure 9. a) Plot of two global fits on experimental data calculated with, and without data at strain rates below 10^{-7} 1/s, extrapolated to geologic strain rates with confidence intervals at 480°C. Fitting error bars on data points are plotted as lines. Data collected at 480°C are highlighted orange. b) Plots of extrapolated viscosity vs. stress to subduction conditions. The grey box indicates viscosity predicted by thermal models of Wada and Wang (2009)

between the flow law and heat flow inferred values is within experimental error, and could be accounted for with a slightly thicker 200-300m weak layer.

5 Conclusions

In this study we redesigned a Griggs-type apparatus and assembly for constant stress creep testing of antigorite at low temperature, low strain rate, and high pressure. Antigorite was tested at temperatures between 75°C and 550°C, by applying 8-12 stress steps per temperature. The microstructure of samples recovered after deformation highlights the importance of basal shear and kinks to antigorite deformation. Deformation data fits well to a barrier-controlled low temperature plasticity flow law, supporting the hypothesis that lattice resistance is the rate-limiting deformation mechanism. When extrapolated to subduction conditions, the data fit surprisingly well to thermal model-based requirements for coupling along the subduction interface.

Open Research

Data associated with this paper are available through the Brown University Digital Repository (<https://doi.org/10.26300/cdn5-he41>)

Acknowledgments

We thank Nicolas Bantut and Emmanuel David for helpful discussions. We would also like to thank Hannah Rabinowitz for discussions and assistance upgrading the apparatus. Cameron Meyers provided a helpful first review of the work. In addition we thank Keishi Okazaki who collected the antigorite used in this study. This work was supported by NSF EAR-1513714 and EAR-2054522.

References

- Amiguet, E., Van De Moortèle, B., Cordier, P., Hilaret, N., & Reynard, B. (2014). Deformation mechanisms and rheology of serpentines in experiments and in nature. *Journal of Geophysical Research: Solid Earth*, 119(6), 4640–4655.
- Auzende, A.-L., Escartin, J., Walte, N. P., Guillot, S., Hirth, G., & Frost, D. J. (2015). Deformation mechanisms of antigorite serpentinite at subduction zone conditions determined from experimentally and naturally deformed rocks. *Earth and Planetary Science Letters*, 411, 229–240.
- Bezacier, L., Reynard, B., Bass, J. D., Sanchez-Valle, C., & Van de Moortèle, B. (2010). Elasticity of antigorite, seismic detection of serpentinites, and anisotropy in subduction zones. *Earth and Planetary Science Letters*, 289(1–2), 198–208.
- Boettcher, M. S., Hirth, G., & Evans, B. (2007). Olivine friction at the base of oceanic seismogenic zones. *Journal of Geophysical Research: Solid Earth*, 112(B1).
- Brantut, N., Baud, P., Heap, M., & Meredith, P. (2012). Micromechanics of brittle creep in rocks. *Journal of Geophysical Research: Solid Earth*, 117(B8).
- Burdette, E. (2021). *Advances in experimental methods and apparatus design applied to investigate the creep and dehydration behavior of antigorite serpentinite* (Doctoral dissertation, Brown University, Providence, RI). Retrieved from <https://doi.org/10.26300/cdn5-he41>
- Chernak, L. J., & Hirth, G. (2010). Deformation of antigorite serpentinite at high temperature and pressure [Journal Article]. *Earth and Planetary Science Letters*, 296(1–2), 23–33. doi: 10.1016/j.epsl.2010.04.035
- David, E. C., Brantut, N., Hansen, L. N., & Mitchell, T. M. (2018). Absence of stress-induced anisotropy during brittle deformation in antigorite serpentinite. *Journal of Geophysical Research: Solid Earth*, 123(12), 10–616.
- David, E. C., Brantut, N., & Hirth, G. (2020). Sliding crack model for nonlinearity and hysteresis in the triaxial stress-strain curve of rock, and application to antigorite deformation. *Journal of Geophysical Research: Solid Earth*, 125(10), e2019JB018970.
- Escartin, J., Hirth, G., & Evans, B. (1997). Effects of serpentinization on the lithospheric strength and the style of normal faulting at slow-spreading ridges [Journal Article]. *Earth and Planetary Science Letters*, 151(3–4), 181–189. doi: 10.1016/S0012-821X(97)81847-X
- Evans, B., & Goetze, C. (1979). The temperature variation of hardness of olivine and its implication for polycrystalline yield stress. *Journal of Geophysical Research: Solid Earth*, 84(B10), 5505–5524.
- Ferrand, T. P., Hilaret, N., Incel, S., Deldicque, D., Labrousse, L., Gasc, J., . . . Schubnel, A. (2017). Dehydration-driven stress transfer triggers intermediate-depth earthquakes [Journal Article]. *Nature Communications*, 8, 15247. doi: 10.1038/ncomms15247
- Frost, H. J., & Ashby, M. F. (1982). *Deformation mechanism maps: the plasticity and creep of metals and ceramics*. Pergamon press.
- Gasc, J., Hilaret, N., Yu, T., Ferrand, T., Schubnel, A., & Wang, Y. (2017). Faulting of natural serpentinite: Implications for intermediate-depth seismicity. *Earth and Planetary Science Letters*, 474, 138–147.
- Grobety, B. (2003). Polytypes and higher-order structures of antigorite: A TEM study. *American Mineralogist*, 88(1), 27–36.
- Gruber, J., Lang, A. C., Griggs, J., Taheri, M. L., Tucker, G. J., & Barsoum, M. W. (2016). Evidence for bulk ripplations in layered solids. *Scientific reports*, 6(1), 1–8.
- Hansen, L. N., David, E. C., Brantut, N., & Wallis, D. (2020). Insight into the microphysics of antigorite deformation from spherical nanoindentation. *Philosophical Transactions of the Royal Society A*, 378(2165), 20190197.

- Hilairt, N., Reynard, B., Wang, Y., Daniel, I., Merkel, S., Nishiyama, N., & Petitgirard, S. (2007). High-pressure creep of serpentinite, interseismic deformation, and initiation of subduction [Journal Article]. *Science*, 318(5858), 1910-3. doi: 10.1126/science.1148494
- Hirauchi, K.-i., Katayama, I., & Kouketsu, Y. (2020). Semi-brittle deformation of antigorite serpentinite under forearc mantle wedge conditions. *Journal of Structural Geology*, 140, 104151.
- Hirth, J. P., Lothe, J., & Mura, T. (1983). Theory of dislocations. *Journal of Applied Mechanics*, 50(2), 476.
- Idrissi, H., Bollinger, C., Boioli, F., Schryvers, D., & Cordier, P. (2016). Low-temperature plasticity of olivine revisited with in situ tem nanomechanical testing. *Science advances*, 2(3), e1501671.
- Idrissi, H., Samaee, V., Lumbeeck, G., van der Werf, T., Pardo, T., Schryvers, D., & Cordier, P. (2020). In situ quantitative tensile testing of antigorite in a transmission electron microscope. *Journal of Geophysical Research: Solid Earth*, 125(3), e2019JB018383.
- King, D., & Marone, C. (2012). Frictional properties of olivine at high temperature with applications to the strength and dynamics of the oceanic lithosphere. *Journal of Geophysical Research: Solid Earth*, 117(B12).
- Kirby, S. H., & Kronenberg, A. K. (1984). Deformation of clinopyroxenite: Evidence for a transition in flow mechanisms and semibrittle behavior. *Journal of Geophysical Research: Solid Earth*, 89(B5), 3177-3192.
- Moarefvand, A., Gasc, J., Fauconnier, J., Baïssat, M., Burdette, E., Labrousse, L., & Schubnel, A. (2021). A new generation griggs apparatus with active acoustic monitoring. *Tectonophysics*, 229032. Retrieved from <https://www.sciencedirect.com/science/article/pii/S0040195121003140> doi: <https://doi.org/10.1016/j.tecto.2021.229032>
- Okazaki, K., Burdette, E., & Hirth, G. (2021). Rheology of the fluid oversaturated fault zones at the brittle-plastic transition. *Journal of Geophysical Research: Solid Earth*, 126(2), e2020JB020804.
- Okazaki, K., & Hirth, G. (2016). Dehydration of lawsonite could directly trigger earthquakes in subducting oceanic crust [Journal Article]. *Nature*, 530(7588), 81-4. doi: 10.1038/nature16501
- Proctor, B., & Hirth, G. (2015). Role of pore fluid pressure on transient strength changes and fabric development during serpentinite dehydration at mantle conditions: Implications for subduction-zone seismicity [Journal Article]. *Earth and Planetary Science Letters*, 421, 1-12. doi: 10.1016/j.epsl.2015.03.040
- Proctor, B., & Hirth, G. (2016). "ductile to brittle" transition in thermally stable antigorite gouge at mantle pressures [Journal Article]. *Journal of Geophysical Research: Solid Earth*, 121(3), 1652-1663. doi: 10.1002/2015jb012710
- Schwartz, S., Guillot, S., Reynard, B., Lafay, R., Debret, B., Nicollet, C., ... Auzende, A. L. (2013). Pressure-temperature estimates of the lizardite/antigorite transition in high pressure serpentinites. *Lithos*, 178, 197-210.
- Shao, T., Zhou, Y., Song, M., Ma, X., Zhang, L., Yao, W., ... Li, J. (2021). Deformation of antigorite and its geological implications. *Journal of Geophysical Research: Solid Earth*, 126(6), e2021JB021650. Retrieved from <https://agupubs.onlinelibrary.wiley.com/doi/abs/10.1029/2021JB021650> (e2021JB021650 2021JB021650) doi: <https://doi.org/10.1029/2021JB021650>
- Syracuse, E. M., van Keken, P. E., & Abers, G. A. (2010). The global range of subduction zone thermal models. *Physics of the Earth and Planetary Interiors*, 183(1-2), 73-90.
- Wada, I., Wang, K., He, J., & Hyndman, R. D. (2008). Weakening of the subduction interface and its effects on surface heat flow, slab dehydration, and mantle wedge serpentinization. *Journal of Geophysical Research: Solid Earth*,

- 113(B4).
- Wada, I., & Wang, K. L. (2009). Common depth of slab-mantle decoupling: Reconciling diversity and uniformity of subduction zones [Journal Article]. *Geochemistry Geophysics Geosystems*, 10. Retrieved from <GotoISI>://WOS:000270942600001 doi: ArtnQ1000910.1029/2009gc002570
- Wicks, F. J., & Whittaker, E. (1977). Serpentine textures and serpentinization. *The Canadian Mineralogist*, 15(4), 459–488.
- Wunder, B., & Schreyer, W. (1997). Antigorite: High-pressure stability in the system mgo-sio₂-h₂o (msh). *Lithos*, 41(1-3), 213–227.

Supporting Information for “Creep Rheology of Antigorite: Experiments at Subduction Zone Conditions”

Eric Burdette and Greg Hirth

¹Department of Earth, Environmental and Planetary Sciences, Brown University, Providence, RI, USA

Contents

1. Text S1 to S4
2. Figures S1 to S5
3. Table S1

Introduction

Here we have included supporting details describing microstructure, calibration, more extensive comparison of our results to other work, and detailed methods used to collect and process strain rate data. In addition we have included the rheological data points and details about the fitting methodology used.

Text S1. Mechanical Data Calculations

The Griggs apparatus has both external load and displacement sensors which need to be corrected to find load and displacement on the sample inside the pressure vessel. Differential stress is determined by subtracting a “hit point” stress (hydrostatic pressure+friction) from the externally measured load. Displacement is determined by subtracting displacement absorbed by the column in compression (Burdette & Hirth, 2020), and referenced relative to the “hit point”.

$$x_{sample} = x_{LVD T2} - \frac{\sigma_{1,external}}{k_{lower_column}} \quad (1)$$

To calculate permanent/inelastic strain, elastic compression of the sample can also be removed:

$$k_{sample} = \frac{E}{l_{sample}} \quad (2)$$

$$x_{inelastic} = x_{LVD T2} - \frac{\sigma_{1,external}}{k_{lower_column}} - \frac{\sigma_{differential,internal}}{k_{sample}} \quad (3)$$

Note that these equations assume sample elasticity is constant, and don’t account for rate-dependent friction.

To calculate strain rates during post-processing, we used the first derivative of a first order Savitzky-Golay filter (moving line fit) over a moving time window chosen for each step. For strain rates above $10^{-6}1/s$, the window could be as short as 100 seconds, while the lowest strain rates require a 10000 second time window. Strain rates chosen for flow law fits were the final point that was not influenced by a disturbance or loading to the next stress. Wherever strain rate is plotted as a continuous function of time (e.g. Figures 3-5), a single window length was chosen over the whole plot to best display data. Data from a slow strain rate step is displayed in Figure S1.

Corresponding author: Eric Burdette, eric_burdette@brown.edu

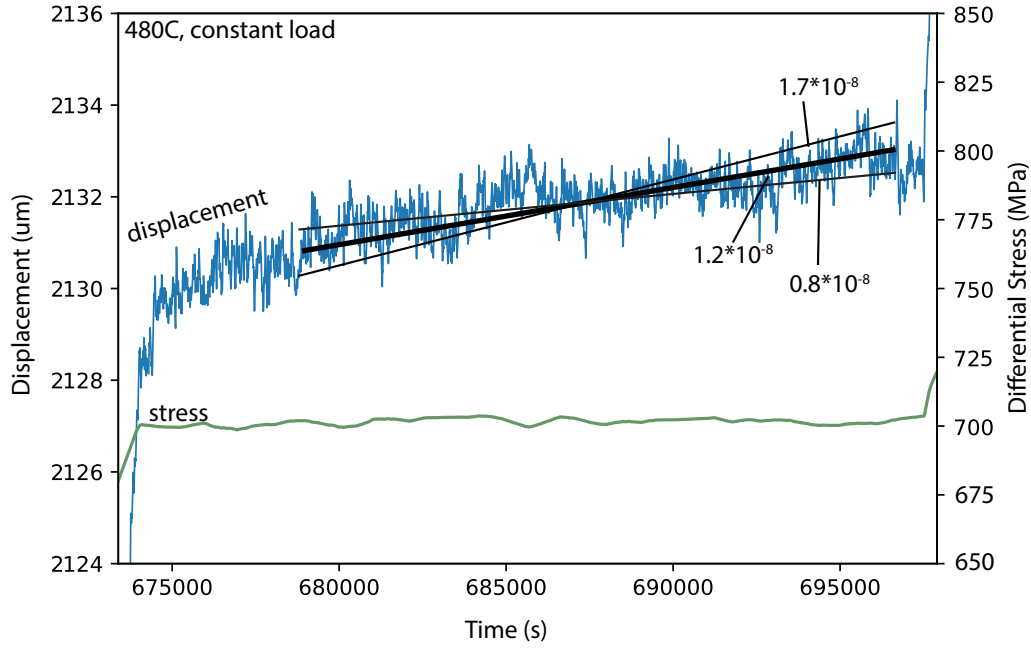


Figure S1. Load and Displacement plotted against time to show strain rate evolution during a stress step. For "low" stresses, the displacement resolution limits determination of strain rate

Text S2. Comparison of Mechanical Data to Other Works

Generally, samples deformed at 1 GPa have very similar strength to our samples as noted in the text.

The samples tested in Hilair et al. (2007) are weaker (50%) than most other published results. The weakness could be a result of several factors, the most notable is the high degree of comminution due to damage during pressurization and repeated compression-tension deformation (Amiguet et al., 2014, Figure 6). In addition, the exponential law recommended after a companion microstructure study (Amiguet et al., 2014) does not extrapolate to low strain rates. Although the dislocation creep fit to data extrapolates reasonably, there is no evidence for dislocation climb or recrystallization in microstructural studies (Amiguet et al., 2014) that would justify its extrapolation.

Text S3. Hardening During Stress Steps

During individual stress steps samples harden over time (Figure 3). Hardening is expected to some extent from other descriptions/results of brittle creep and high temperature creep tests where primary, secondary, and tertiary creep phases can be identified. For westerly granite calibration tests (Figure 2), at each step samples reach constant strain rates after relatively small strains (0.2%). Post-processing of antigorite data shows that it may continue to harden after similar 0.2% strain steps (Figure 3).

Text S4. Flow Law Fit Methodology

A low temperature plasticity flow law was fit to stress vs. $\log(\text{strainrate})$ using a Markov-chain Monte-Carlo (MCMC-NUTS via PyMC3) optimizer due to the small lo-

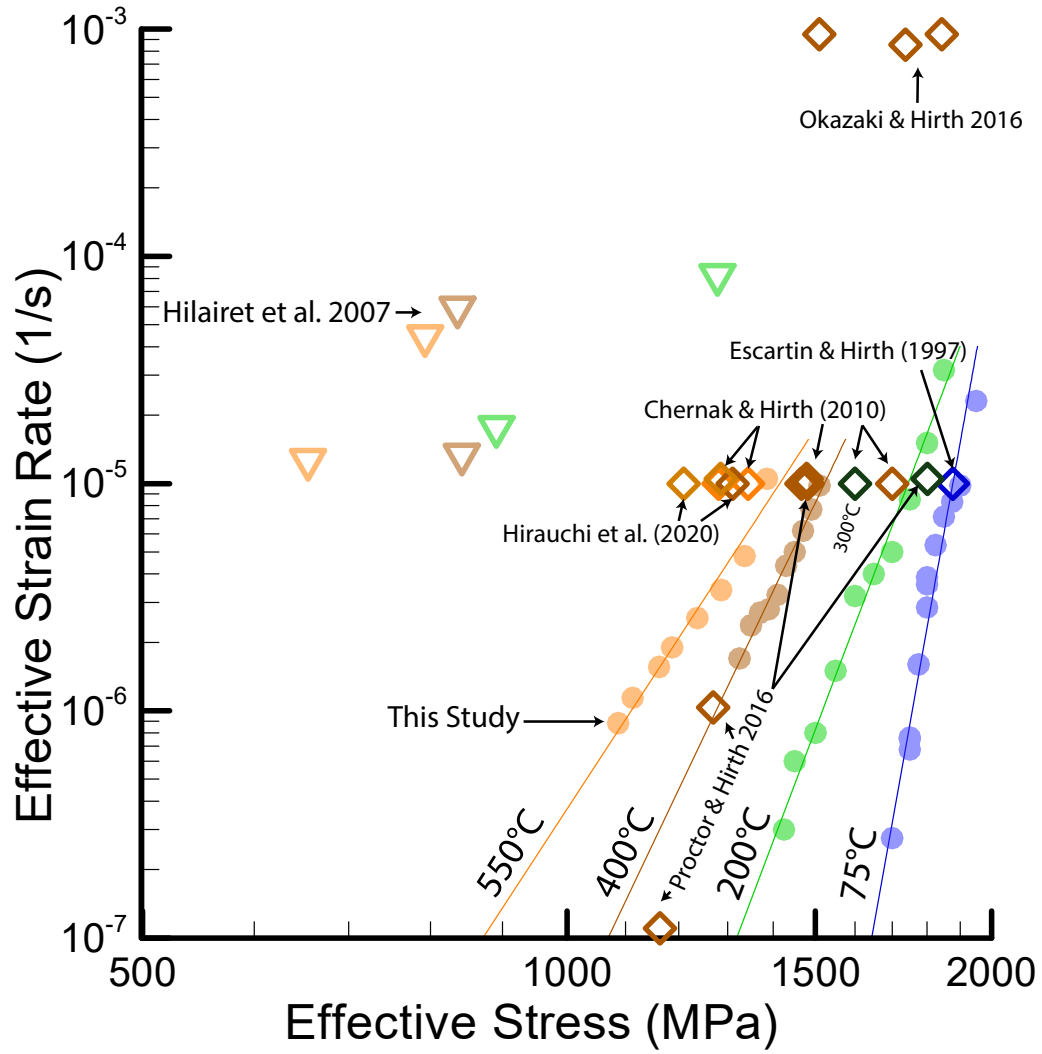


Figure S2. Compilation of other high pressure experimental antigorite deformation results plotted over results from the current study. Colors of points denotes temperature for all points. Both cores (Hirauchi et al., 2020; Chernak & Hirth, 2010; Escartin et al., 1997) and gouge (Chernak & Hirth, 2010; Proctor & Hirth, 2016; Okazaki & Hirth, 2016) are plotted.

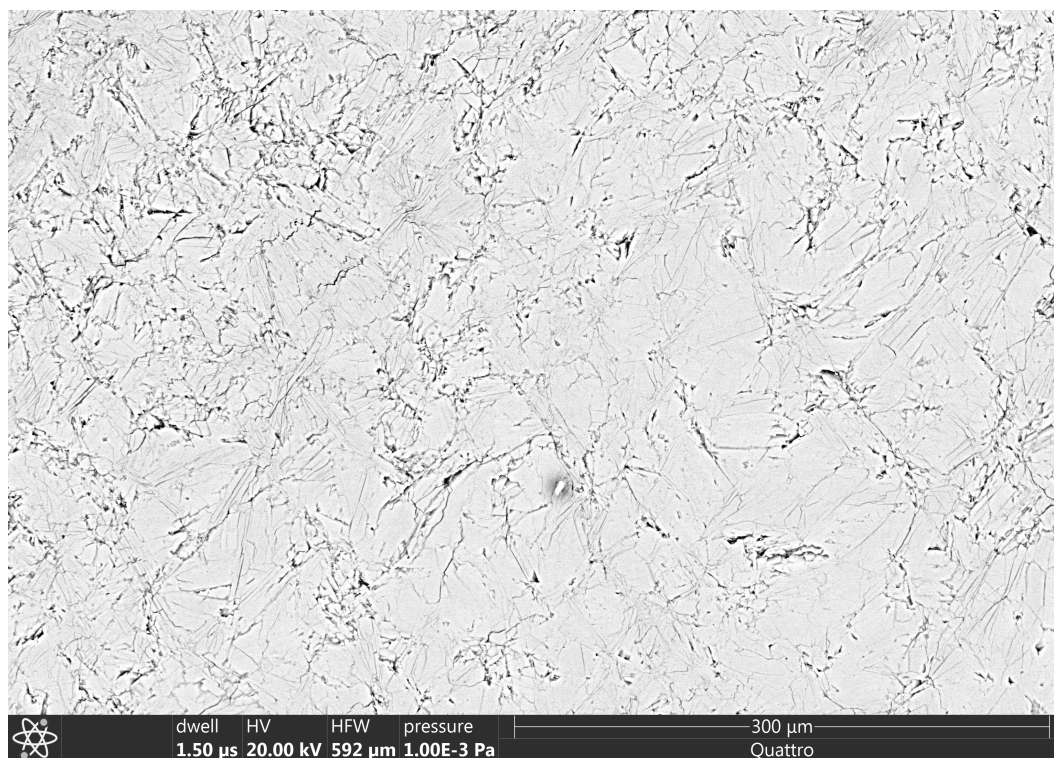


Figure S3. SEM image of intermediate zoom and multiple intersections at 200°C. Voids are present due to grain pull-out during polishing. The featured intersection is near the top left corner.

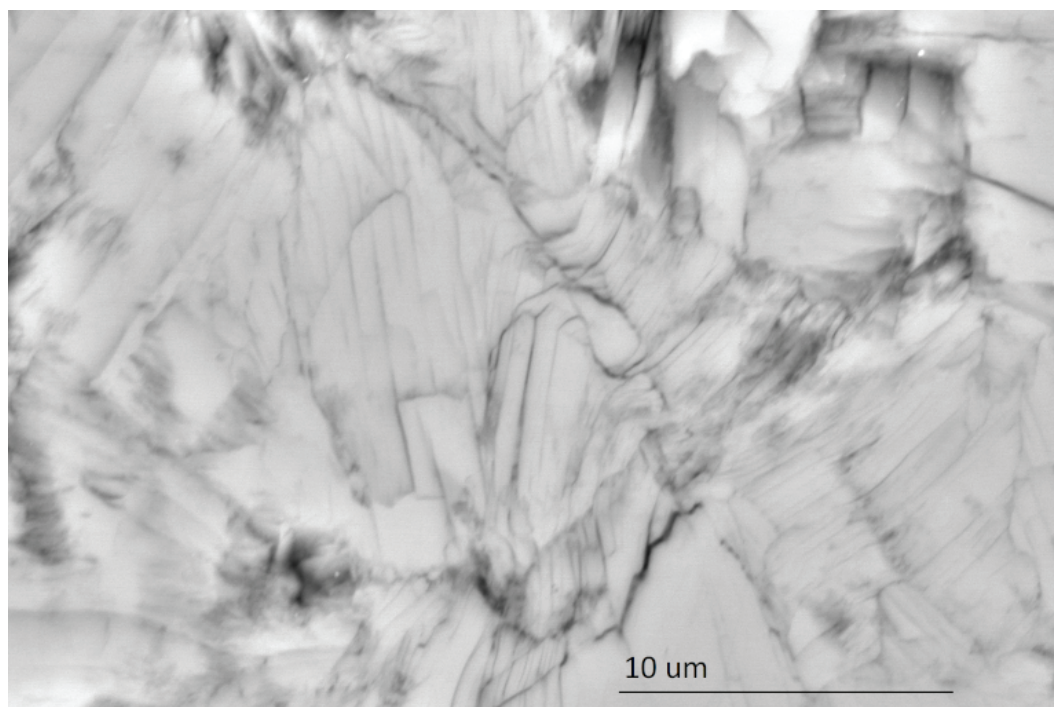


Figure S4. Gentle curvature of sheets recovered from 550°C sample.

cal discontinuities in the fit. Stress and strain error were included in the fit with input distributions of ± 40 MPa and $3 - 1.5x$ 1/s centered around each point. Results with errors are presented in Table 2 and distributions of the posterior are plotted in Figure S5. 400000 samples were taken across 50 chains after burn-in to ensure accuracy of the fit. The upper and lower highest density intervals are included in addition to the standard deviation intervals because they contain information about the skewness of the distribution if it is not exactly Gaussian.

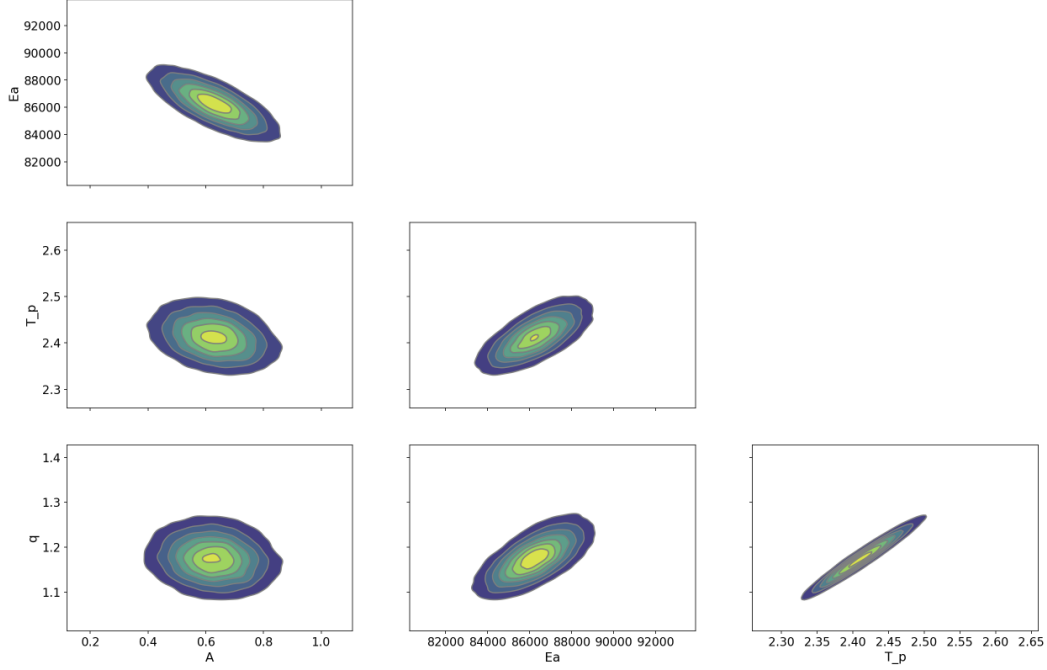


Figure S5. Posterior probability density functions in parameter space for the MCMC fit.

Low stress data have a larger influence on the extrapolated fit because they define the transition between defect density and temperature activation dominated regions of the low temperature plasticity flow law. The start of this transition can be seen in the slight curvature of the fit around points at 480°C in Figure 5b. In the LTP flow law, the region is defined by exponents p , q , and normalization factor τ_p . Below the transition at low stresses, the external term with σ^2 (proportional to defect density) dominates stress dependence.

Table 1: Creep data

Initial Strainrate (1/s)	Final Strainrate (1/s)	Initial Strain	Final Strain	Stress (MPa)	T (°C)	Experiment
6.80E-06	3.60E-06	0.0064	0.01	1800	75	W2441
9.40E-06	5.36E-06	0.01	0.016	1825	75	W2441
1.30E-05	7.15E-06	0.016	0.024	1850	75	W2441
1.42E-05	8.30E-06	0.024	0.034	1875	75	W2441
1.60E-05	9.80E-06	0.034	0.05	1900	75	W2441
3.00E-05	2.31E-05	0.05	0.07	1950	75	W2441
8.00E-07	3.00E-07	0.00042	0.00087	1425	200	W2447
1.00E-06	6.00E-07	0.00087	0.0011	1450	200	W2447

Continuation of Table 1						
1.00E-06	8.00E-07	0.0011	0.00178	1500	200	W2447
2.20E-06	1.50E-06	0.00178	0.00268	1550	200	W2447
5.00E-06	3.20E-06	0.00268	0.00338	1600	200	W2447
7.00E-06	4.00E-06	0.00338	0.00423	1650	200	W2447
1.10E-05	5.00E-06	0.00423	0.00559	1700	200	W2447
1.30E-05	8.51E-06	0.00559	0.0071	1750	200	W2447
2.60E-05	1.51E-05	0.0071	0.0096	1800	200	W2447
5.20E-05	3.16E-05	0.0096	0.0148	1850	200	W2447
2.25E-06	1.70E-06	0.0055	0.007	1325	400	W2439
2.80E-06	2.38E-06	0.007	0.009	1350	400	W2439
3.40E-06	2.70E-06	0.009	0.011	1370	400	W2439
3.80E-06	2.80E-06	0.011	0.0133	1390	400	W2439
4.00E-06	3.24E-06	0.0133	0.016	1410	400	W2439
5.00E-06	4.35E-06	0.016	0.019	1430	400	W2439
6.90E-06	5.00E-06	0.019	0.023	1450	400	W2439
7.80E-06	6.20E-06	0.023	0.028	1470	400	W2439
9.40E-06	7.70E-06	0.028	0.0325	1490	400	W2439
1.05E-05	9.80E-06	0.0325	0.036	1510	400	W2439
1.40E-06	8.82E-07	0.0005	0.00138	1062	550	W2424
1.60E-06	1.14E-06	0.00138	0.0024	1088	550	W2424
3.00E-06	1.56E-06	0.0024	0.00373	1137	550	W2424
2.60E-06	1.90E-06	0.00373	0.00474	1162	550	W2424
5.40E-06	2.56E-06	0.00474	0.00705	1212	550	W2424
7.50E-06	3.40E-06	0.00705	0.0106	1261	550	W2424
9.00E-06	4.80E-06	0.0106	0.015	1311	550	W2424
1.40E-05	1.05E-05	0.015	0.023	1361	550	W2424
8.00E-09	5.00E-09	0.0001	0.001	480	520	W2520
2.20E-08	1.70E-08	0.001	0.0022	600	520	W2520
4.00E-08	3.40E-08	0.0022	0.0033	690	520	W2520
8.00E-08	6.00E-08	0.0033	0.0048	790	520	W2520
9.50E-08	7.50E-08	0.0048	0.0063	880	520	W2520
5.00E-09	4.50E-09	0.0063	0.0067	470	520	W2520
1.40E-07	1.20E-07	0.0067	0.018	970	520	W2520
1.41E-09	1.40E-09	0.0001	0.0003	1230	76	W2521
4.00E-09	2.50E-09	0.0003	0.0005	1280	76	W2521
8.00E-08	5.00E-09	0.0005	0.0008	1330	76	W2521
2.50E-08	1.50E-08	0.0008	0.0015	1380	76	W2521
5.00E-08	3.00E-08	0.0015	0.0028	1430	76	W2521
2.50E-07	6.00E-08	0.0028	0.0046	1480	76	W2521
1.60E-06	1.50E-07	0.0046	0.00758	1550	76	W2521
1.50E-06	3.00E-07	0.00758	0.011	1580	76	W2521
2.00E-06	6.00E-07	0.011	0.0147	1600	76	W2521
2.20E-06	5.00E-07	0.0147	0.0198	1650	76	W2521
3.30E-06	1.00E-06	0.0198	0.022	1700	76	W2521
9.00E-06	2.00E-06	0.022	0.0257	1750	76	W2521
1.20E-05	5.00E-06	0.0257	0.032	1800	76	W2521
7.00E-08	1.50E-08	0.0001	0.0002	635	480	W2526
5.00E-09	2.50E-09	0.0002	0.0005	475	480	W2526
1.00E-08	7.50E-09	0.0005	0.001	575	480	W2526
1.20E-08	1.00E-08	0.001	0.0013	645	480	W2526
3.00E-08	2.50E-08	0.0013	0.0021	725	480	W2526
2.00E-07	1.50E-07	0.0021	0.0028	975	480	W2526
8.00E-09	5.00E-09	0.0028	0.0032	505	480	W2526
1.50E-08	9.00E-09	0.0032	0.0036	595	480	W2526

Continuation of Table 1						
1.90E-08	1.50E-08	0.0036	0.004	695	480	W2526
3.50E-08	3.00E-08	0.004	0.0044	795	480	W2526
End of Table						

References

- Amiguet, E., Van De Moortèle, B., Cordier, P., Hilaret, N., & Reynard, B. (2014). Deformation mechanisms and rheology of serpentines in experiments and in nature. *Journal of Geophysical Research: Solid Earth*, *119*(6), 4640–4655.
- Burdette, E., & Hirth, G. (2020). Enhanced dehydration weakening of antigorite driven by slow shear heating: Insights from high-pressure experiments with a modified apparatus stiffness. *Journal of Geophysical Research: Solid Earth*, *125*(11), e2020JB020064.
- Chernak, L. J., & Hirth, G. (2010). Deformation of antigorite serpentinite at high temperature and pressure [Journal Article]. *Earth and Planetary Science Letters*, *296*(1-2), 23-33. doi: 10.1016/j.epsl.2010.04.035
- Escartin, J., Hirth, G., & Evans, B. (1997). Effects of serpentinization on the lithospheric strength and the style of normal faulting at slow-spreading ridges [Journal Article]. *Earth and Planetary Science Letters*, *151*(3-4), 181-189. doi: 10.1016/S0012-821x(97)81847-X
- Hilaret, N., Reynard, B., Wang, Y., Daniel, I., Merkel, S., Nishiyama, N., & Petitgirard, S. (2007). High-pressure creep of serpentine, interseismic deformation, and initiation of subduction [Journal Article]. *Science*, *318*(5858), 1910-3. doi: 10.1126/science.1148494
- Hirauchi, K.-i., Katayama, I., & Kouketsu, Y. (2020). Semi-brittle deformation of antigorite serpentinite under forearc mantle wedge conditions. *Journal of Structural Geology*, *140*, 104151.
- Okazaki, K., & Hirth, G. (2016). Dehydration of lawsonite could directly trigger earthquakes in subducting oceanic crust [Journal Article]. *Nature*, *530*(7588), 81-4. doi: 10.1038/nature16501
- Proctor, B., & Hirth, G. (2016). “ductile to brittle” transition in thermally stable antigorite gouge at mantle pressures [Journal Article]. *Journal of Geophysical Research: Solid Earth*, *121*(3), 1652-1663. doi: 10.1002/2015jb012710